IOPscience iopscience.iop.org

Home Search Collections Journals About Contact us My IOPscience

On the sol–gel synthesis and thermal, structural, and magnetic studies of transition metal (Ni, Co, Mn) containing ZnO powders

This article has been downloaded from IOPscience. Please scroll down to see the full text article.

2006 J. Phys.: Condens. Matter 18 2473

(http://iopscience.iop.org/0953-8984/18/8/012)

View the table of contents for this issue, or go to the journal homepage for more

Download details:
IP Address: 129.252.86.83
The article was downloaded on 28/05/2010 at 09:00

Please note that terms and conditions apply.

INSTITUTE OF PHYSICS PUBLISHING JOURNAL OF PHYSICS: CONDENSED MATTER

J. Phys.: Condens. Matter **18** (2006) 2473–2486 doi:10.1088/0953-8984/18/8/012

On the sol–gel synthesis and thermal, structural, and magnetic studies of transition metal (Ni, Co, Mn) containing ZnO powders

Subhash Thota, Titas Dutta and Jitendra Kumar[1]

Materials Science Programme, Indian Institute of Technology Kanpur, Kanpur-208016, India

E-mail: jk@iitk.ac.in

Received 16 September 2005, in final form 28 December 2005
Published 10 February 2006
Online at stacks.iop.org/JPhysCM/18/2473

Abstract

Transition metal containing ZnO powders ($Zn_{1-x}M_xO$, $0 \leqslant x \leqslant 0.30$; M = Ni, Mn, Co) have been synthesized by a sol–gel process using zinc acetate dihydrate, respective acetate and oxalic acid as precursors with ethanol as a solvent. The process essentially involves gel formation, drying at 80 °C for 24 h to provide the oxalate, and calcination at 500 °C for 2 h to undergo an exothermic reaction and yield $Zn_{1-x}M_xO$ powder. Their XRD patterns correspond to a wurtzite hcp structure similar to that of pure ZnO, but with the lattice parameters varying slightly with type and extent of doping. It is shown that the dissolution of nickel and cobalt in ZnO is less than 10 at.%, whereas that of manganese lies between 10 and 15 at.%. Other phases that emerge include NiO (hexagonal, $a = 2.954$ Å, $c = 7.236$ Å), $ZnCo_2O_4$ (cubic, $a = 8.094$ Å) and $ZnMnO_3$ (cubic, $a = 8.35$ Å) in the Ni, Co and Mn containing ZnO systems, respectively. Observations of hysteresis loops both at 10 and 320 K and the nature of ESR spectra provide evidence for the ferromagnetic state in nickel containing ZnO powder. Besides, the deviation occurs in the magnetization versus temperature curves in zero field cooled (ZFC) and field cooled (FC) conditions (blocking temperature T_B being 32 K for 5 at.% Ni). The magnetic behaviour of manganese and cobalt doped zinc oxide is, however, different, namely, (i) no hysteresis loops, (ii) decrease in magnetization with increase of Mn or Co content, and (iii) identical M–T curves under ZFC and FC conditions. The inverse susceptibility versus temperature curves of $Zn_{1-x}Mn_xO$ compounds reveal ferrimagnetism with Néel temperature T_N of 4 K for $x = 0.02$, but antiferromagnetism for $x = 0.15$ and 0.25 with Curie–Weiss temperature of −43 and −30 K, respectively.

[1] Author to whom any correspondence should be addressed.

 © 2006 IOP Publishing Ltd Printed in the UK

1. Introduction

Diluted magnetic semiconductors (DMSs) have attracted immense interest in the recent past because of their potential application in spintronic devices [1–10]. They utilize both the charge and the spin of electrons and exhibit novel combination of semiconducting and magnetic properties. A DMS is essentially a semiconductor with dilute dispersion of a magnetic species, e.g., different semiconductor materials explored include II–VI (namely, CdTe, ZnSe, ZnO) and III–V (namely, GaAs, InAs, InP) compounds with magnetic impurities Mn, Co, Ni, or Fe [7–14]. However, the Curie temperature found is generally too low to have any significant practical impact. The Dietl *et al* [3] theoretical prediction of room temperature ferromagnetism in a wide band gap semiconductor such as ZnO, doped with manganese, opened a new field for investigation. Consequently, several researchers initiated studies on zinc oxide based DMSs, taking transition metals as magnetic dopants. But, the reports that emanated in a short time span are quite inconsistent. For example, while Sharma *et al* [15, 16] and Heo *et al* [17] have reported ferromagnetism much above room temperature in Mn doped ZnO, others found either much lower ferromagnetic ordering temperature [18–21] or no ferromagnetism at all above 4 K for any 3d transition metal [22–25]. The inconsistent results further suggest that the ferromagnetic ordering is extremely sensitive to the synthesis route, conditions, and product form (bulk, powder or thin films). Recently, Gamelin's group has employed a solution based synthetic route to produce $Zn_{1-x}M_xO$ ($M = Ni^{2+}$, Mn^{2+}, Co^{2+}) DMSs and shown the presence of ferromagnetism above room temperature in them [26–29]. Lee *et al* [30] have adopted the sol–gel process for the synthesis of $Zn_{1-x}Co_xO$ ($0 < x < 0.25$) thin films that exhibit ferromagnetic behaviour with a Curie temperature higher than 350 K. Also, Cong *et al* [31] observed room temperature ferromagnetism in Mn doped ZnO nanoparticles, produced by a rheological phase reaction precursor method. Pearton *et al* [8] have recently reviewed the progress about the issues involving control doping of transition metals and resulting ferromagnetism in ZnO based systems. Also, ZnO has assumed significance because of its potential industrial applications in UV-light emitters, varistors, gas sensors, transparent electronics, surface acoustic wave devices, piezoelectric transducers, window materials for display and solar cells besides becoming a prime candidate for incorporating the spin functionality to develop magnetic FETs, low threshold spin-lasers, etc [8–10].

Despite a number of reports available, confusion still persists on the existence and origin of room temperature ferromagnetism in ZnO based DMSs [7–10]. Hence, an attempt is made to reinvestigate $Zn_{1-x}M_xO$ ($0 < x < 0.30$; M = Ni, Mn, Co). For synthesis, the sol–gel method has been chosen because it is cost effective, requires low temperature for processing, allows higher degree of solubility, provides homogeneous dispersion of dopants and has the advantage of controlling the composition accurately [32]. The powder products have been characterized with regard to their thermal stability (TGA/DTA), phase(s) (XRD), microstructure (SEM), and magnetic properties (VSM, SQUID and ESR).

2. Experimental details

For synthesis of the transition metal containing zinc oxide, zinc acetate dihydrate and respective acetates, $M(CH_3COO)_2{\cdot}4H_2O$ with M = Ni, Co, or Mn, are first dissolved in appropriate amounts and subjected to stirring for 3 h at 80 °C to obtain a transparent sol. Oxalic acid solution (250 ml) is then added slowly to the warm transparent sol and stirred continuously to yield a thick yellowish white gel. The gel product is subsequently dried at 80 °C for 24 h, ground, sieved through 240 mesh, calcined at 500 °C for 2 h and cooled at a rate of 10 °C min^{-1}.

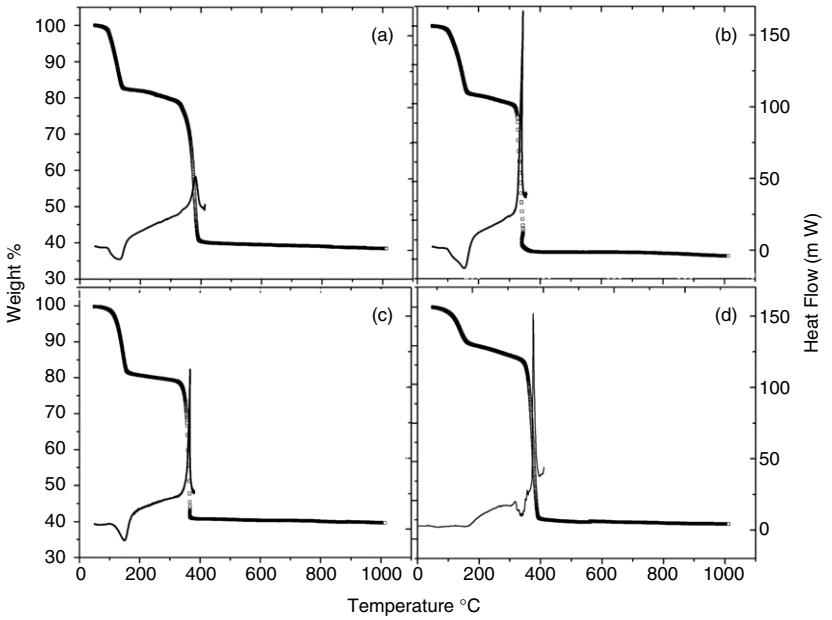

Figure 1. Thermogravimetric and differential thermal analysis plots of (a) pure ZnO, (b) $Zn_{0.8}Co_{0.2}O$, (c) $Zn_{0.8}Mn_{0.2}O$, and (d) $Zn_{0.8}Ni_{0.2}O$ compounds.

This process gives a fine powder. The compounds of composition $Zn_{1-x}M_xO$ (M = Ni, Co, Mn) with x varying from 0.02 to 0.30 have been prepared under identical conditions. The above procedure was repeated without the transition metal acetates to obtain pure ZnO powder [33, 34]. Thermal analysis of the products was carried out with a Perkin Elmer Pyres Diamond thermogravimetric/differential thermal analysis (TG/DTA) system. An x-ray powder diffractometer (Rich Seifert model ISO Debye flux 2002) was used for x-ray diffraction (XRD) and identification of the phase(s), and a vibrating sample magnetometer (Princeton VSM model −150) and SQUID magnetometer (Quantum Design) were employed for magnetic characterization. Also, electron paramagnetic resonance spectra at room temperature were recorded using a Bruker EMX EPR spectrometer model 1444 in the X-band. A scanning electron microscope (FEI Quanta 200HV) was used for observing the microstructure and morphology.

3. Results and discussions

3.1. Thermal analysis

To investigate the thermal stability of the oven dried precursor of $Zn_{1-x}M_xO$ (M = Ni, Mn, Co; $x = 0.2$), its weight was monitored with heating at the rate of 10 °C min^{-1} in oxygen ambient up to 1000 °C. In all the samples, three main stages of weight loss are observed (figure 1). Table 1 summarizes the values of weight loss and other related parameters. For the case of pure ZnO, the first stage of thermal decomposition occurs in the temperature range 99–155 °C and corresponds to a weight loss of ∼17%. This endothermic reaction was also observed by Pillai *et al* [32], Shen *et al* [34], and Guo *et al* [35], who prepared pure ZnO powder by decomposition of zinc oxalate dihydrate, $ZnC_2O_4{\cdot}2H_2O$. The weight loss is attributed to removal of crystallizing water (partly or wholly) of $ZnC_2O_4{\cdot}2H_2O$. The differential thermal

Table 1. TGA/DTA data, average particle size and colour of $Zn_{1-x}M_xO$ (M = Ni, Co, Mn) nanocrystalline powders synthesized by the sol–gel process for $x = 0$ and 0.20.

Composition	Weight change (%)	Temperature range (°C)	Position of maximum weight change (°C) T_1	T_2	Rate of weight loss (mg/(°C)) at T_2	Temperature range for endothermic/ exothermic peaks(°C)	Particle size (nm)	Colour before and after calcination
ZnO	17.3 49.3 4.8	84–146 392–405 408–1000	84	381	0.029	128–143 378–402	15.9	White–yellowish white
$Zn_{0.8}Co_{0.2}O$	17.9 47.4 1.6	91–184 315–367 386–1000	149	327	0.075	95–182 317–350	16.6	Pink–green
$Zn_{0.8}Mn_{0.2}O$	18.5 47.8 3.1	102–165 323–367 383–1011	142	358	0.052	112–162 330–365	18.9	White–dark grey
$Zn_{0.8}Ni_{0.2}O$	9.6 47.5 2.8	105–176 335–400 418–1016	139	379	0.028	112–163 279–307	17.8	Green–grey

analysis (DTA) plot also shows a well defined endothermic peak around 128 °C, corresponding to loss of crystallizing water. If all the water is removed, a weight loss of about 19% is expected. As the loss observed is about 17%, it is believed that a small amount of crystallizing water still remains with the zinc oxalate. Further evidence to this fact is found in the FTIR spectrum which shows the signature of OH bonds. In the second stage, weight loss takes place quite rapidly in the temperature range of 329–405 °C; the reaction is exothermic in nature and yields mainly ZnO. Needless to say, anhydrous zinc oxalate on giving off ZnO should undergo a weight loss of 47% as against 47.6% observed in the present case. The third stage appears above 407 °C in which the remaining volatile species come out; the weight loss is ∼4.8%. The final weight of the product is about 40% of the original and is similar to expectation in any sol–gel reaction [36]. Since no appreciable change in weight is observed above 450 °C, the calcination temperature for the product is optimized at 500 °C. The behaviour of cobalt and manganese containing powder samples is similar to that of pure ZnO. However, in nickel containing ZnO, the loss of crystallizing water occurs in two substages, the temperature being 142 °C and 297 °C. The colour of the various powder samples as synthesized and after the calcination process is given in table 1 (notice changes in colour with the transition metal and its concentration).

3.2. Phase evaluation and microstructure

Figure 2(a) shows the XRD patterns of as-prepared pure ZnO powder before and after calcination at 200 and 500 °C for 2 h each. These patterns may be associated with $ZnC_2O_4{\cdot}2H_2O$, $ZnC_2O_4{\cdot}xH_2O$ and ZnO, respectively. The XRD pattern obtained after calcination at 500 °C for 2 h is well defined and corresponds to the wurtzite hcp structure with $a = 3.248 \pm 0.005$ Å and $c = 5.203 \pm 0.005$ Å, and $Z = 2$ of pure ZnO, the known lattice parameters being $a = 3.249$ Å, $c = 5.205$ Å [37]. The peaks of aluminium are arising due to the sample holder used as standard for calibration. In the case of $Zn_{1-x}Ni_xO$, the sample continues to retain the wurtzite hcp structure, but the lattice parameters differ and decrease slightly with increase of the nickel

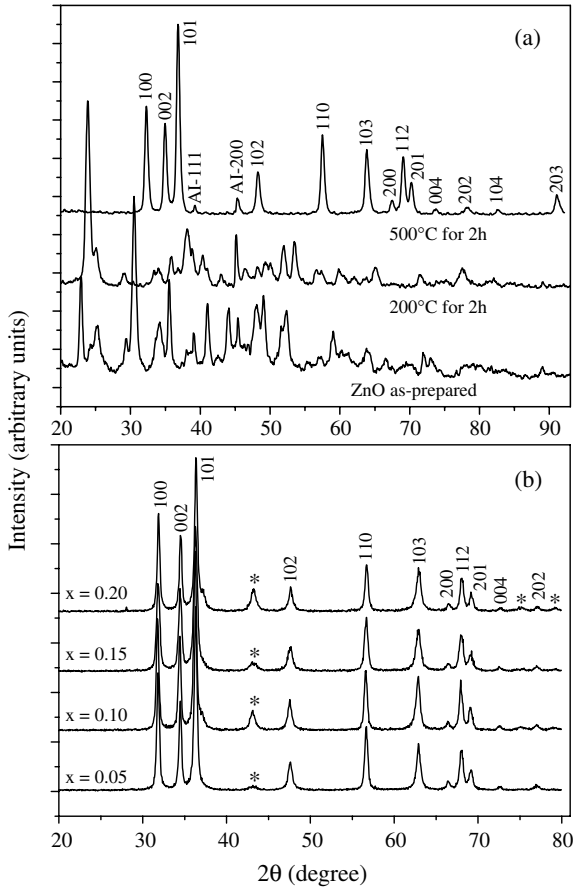

Figure 2. XRD patterns of (a) pure ZnO and (b) $Zn_{1-x}Ni_xO$ for $x = 0.05$–0.20; the diffraction peaks corresponding to hexagonal NiO phase are indicated with an asterisk (∗).

content (x). Since the ionic radius of Ni^{2+} is slightly less than that of the Zn^{2+} ion in tetrahedral coordination (0.55 Å and 0.60 Å, respectively [38]), spectroscopic evidence exists for transition metal ions assuming tetrahedral sites in the wurtzite structure of ZnO over a wide solubility range [7, 23, 25, 39, 40], and the lattice parameters decrease with increase in nickel content (e.g., ∼2.5% decrease in unit cell volume for $x = 0.05$), Ni^{2+} ions are possibly getting incorporated in the ZnO matrix itself. This conjecture is further supported later by the absence of any secondary amorphous or crystalline phase in the microstructure under TEM. Beyond 10 at.% nickel content, characteristic XRD peaks of NiO (hexagonal; lattice parameters $a = 2.954$ Å, $c = 7.236$ Å) also appear (figure 2(b)). This suggests that the dissolution of nickel in ZnO is less than 10 at.%. The intensity of the nickel oxide peak increases with increasing nickel content. The average particle size estimated from the Scherrer formula and BET surface area measurements for $Zn_{1-x}Ni_xO$ powder falls in the nanometre regime, values being 15 and 19 nm, respectively, for $x = 0.2$.

Cobalt containing ZnO samples continue to retain the wurtzite hcp structure with lattice parameters increasing marginally with increase in cobalt content. However, at 10 at.%, the presence of $ZnCo_2O_4$ (cubic, $a \approx 8.0946$ Å) is detected (figure 3(a)). With further increase of

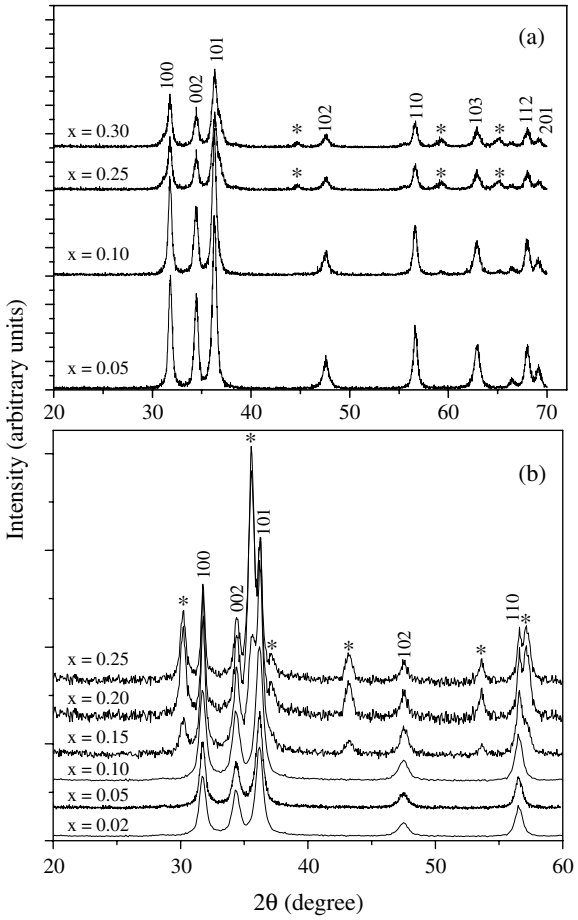

Figure 3. XRD patterns of (a) $Zn_{1-x}Co_xO$ and (b) $Zn_{1-x}Mn_xO$ for various values of x; diffraction peaks marked with an asterisk (∗) represent $ZnCo_2O_4$ and $ZnMnO_3$ in (a) and (b), respectively.

cobalt content, peaks corresponding to $ZnCo_2O_4$ rise progressively. These results suggest that the dissolution of cobalt in ZnO is less than 10 at.%. In contrast to cobalt, manganese doping causes slightly large increase in lattice parameters. This is possibly due to large size of Mn^{2+} ion in comparison to Zn^{2+}, the ionic radii of Mn^{2+} and Zn^{2+} in tetrahedral coordination being 0.66 and 0.60 Å, respectively [38]. This finding in the powder samples is consistent with the increase in c-parameter observed in $Zn_{1-x}Mn_xO$ layers grown on sapphire by molecular beam epitaxy [41]. Extra peaks begin appearing at 15 at.% doping. So, the dissolution of Mn in ZnO is in between 10 and 15 at.%. The extra peaks correspond to $ZnMnO_3$ having a cubic structure with $a \approx 8.35$ Å. The amount of this phase increases progressively (figure 3(b)) with manganese content beyond 15 at%. Figure 4 shows a few typical scanning electron micrographs (recorded in SE-mode) of the microstructure at various stages of synthesis. The gel immediately after formation depicts a filter paper like fibrous network (figure 4(a)). When the alcohol has evaporated and a few hours have elapsed, the gel becomes viscous. Its microstructure then reveals the emergence of numerous needles distributed all over uniformly (figure 4(b)). After drying the gel at 80 °C for 24 h, rods of nearly the same diameter (180–200 μm) but of various lengths appear. On examining very closely, one finds them to consist of a number of

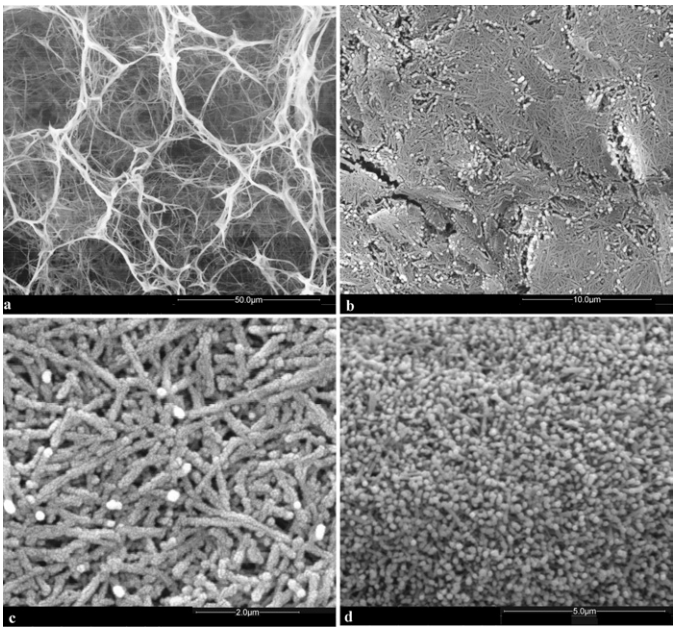

Figure 4. Typical SEM secondary electron images of pure ZnO at various stages; (a) as-prepared gel, (b) after a few hours, (c) after drying at 80 °C for 24 h, and (d) after calcination at 500 °C for 2 h.

particles disposed along the length (figure 4(c)). Some particles lying independently can also be seen in figure 4(c). This product has been ground, sieved through 240 mesh and calcined at 500 °C for 2 h. Figure 4(d) shows the morphology and distribution of pure ZnO agglomerated particles. These features are prevalent in both the nickel and cobalt doped ZnO synthesis too. However, in the case of $Zn_{1-x}Mn_x$ O, the morphology of the gel after drying at 80 °C for 24 h is very different (figure 5). It shows emergence of needle shaped crystals of various dimensions with sharp boundaries. Transmission electron microscopic observations of transition metal containing ZnO powders (calcined at 500 °C for 2 h and used for further studies) provide no evidence of any secondary amorphous phase or nanosized metallic particles or compounds. These observations suggest too that the metallic species are getting dissolved in the ZnO matrix itself.

3.3. Magnetic characterization

Magnetization (M) versus field (H) plots for $Zn_{1-x}Ni_xO$ ($x = 0.05, 0.15, 0.25$) samples calcined at 500 °C for 2 h are shown in figure 6. The values of their saturation magnetization (M_s), coercive field (H_c) and other related parameters are summarized in table 2. Accordingly, the saturation magnetization (M_s) value for all the compositions lies in the range of 1.407–2.861 emu g^{-1} at 10 K and increases with increase of nickel content. Also, the coercivity (H_c) progressively increases with the nickel content, the values being in the range 660–879 Oe for $x = 0.05$–0.25. Above room temperature (320 K), the M_s value is just 0.18 emu g^{-1} for $Zn_{0.85}Ni_{0.15}O$, i.e., less than half that measured at 10 K. The plots indicate the ferromagnetic nature of the nickel doped zinc oxide both at 10 and 320 K. This is further confirmed by room temperature ferromagnetic resonance (FMR) signals observed in the EPR spectra (figure 7).

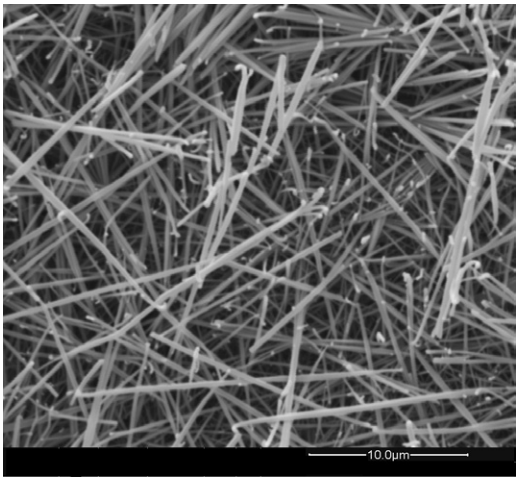

Figure 5. SEM secondary electron image showing the morphology of a gel after drying at 80 °C for 24 h in the $Zn_{1-x}Mn_xO$ system for $x = 0.25$.

Table 2. Saturation magnetization (M_s), remanence (M_r), coercivity (H_c) and (M_r/M_s) ratio values of $Zn_{1-x}Ni_xO$ ($x = 0.05, 0.15, 0.25$) at 10 and 320 K.

System	T (K)	H_c (Oe)	M_s (emu g^{-1})	M_r (emu g^{-1})	M_r/M_s (%)
$Zn_{0.95}Ni_{0.05}O$	10	660	1.407	0.118	8.4
$Zn_{0.85}Ni_{0.15}O$	10	793	1.661	0.128	7.7
$Zn_{0.75}Ni_{0.25}O$	10	879	2.861	0.200	7.0
$Zn_{0.95}Ni_{0.5}O$	320	194	0.180	0.038	21.1
$Zn_{0.85}Ni_{0.15}O$	320	219	0.218	0.042	19.3
$Zn_{0.75}Ni_{0.25}O$	320	267	0.988	0.054	54.6

Clearly, there is a shift in the magnetic resonance absorption spectrum towards a lower field with increase of nickel content. This can be ascribed to an increase in the ferromagnetic interaction between nickel ions as the average distance between them is expected to decrease with increase in x. The FMR spectrum shows a typical shift of ∼460 Oe for the case of $x = 0.25$ from the free electron position (3373 Oe), the corresponding g-factors being 2.317 and 2.0023. This clearly suggests that Ni doped ZnO samples prepared by sol–gel process and calcined at 500 °C for 2 h are ferromagnetic in nature at room temperature. The only report which suggests high-T_C ferromagnetism in Ni containing ZnO is of Radovanovic *et al* [26], who used a solution method for their preparation. Accordingly, colloidal Ni^{2+}:ZnO nanocrystals exhibit paramagnetism but their aggregation gives rise to ferromagnetism with $T_C > 350$ K, increase in domain volume and emergence of crystal defects. Also, the saturation magnetization of 5% Ni containing ZnO samples is around 0.18 emu g^{-1} at 320 K as compared to the value ∼0.03 emu g^{-1} found in 0.93% Ni^{2+}:ZnO nanocrystals at 350 K [26].

Figure 8 shows the temperature-dependent magnetization $M(T)$ of both field cooled (FC) and zero field cooled (ZFC) $Zn_{1-x}Ni_xO$ powder samples at 500 Oe. In the ZFC case, the sample is first cooled under zero applied field to 10 K and then the net magnetization is measured while heating the sample at a constant rate (10 K min^{-1}) at a small uniform external field of 500 Oe. For nanosized particles the M–T curve has a characteristic shape, similar to that shown in figure 8. Upon cooling, each particle tends to magnetize along the preferred crystal

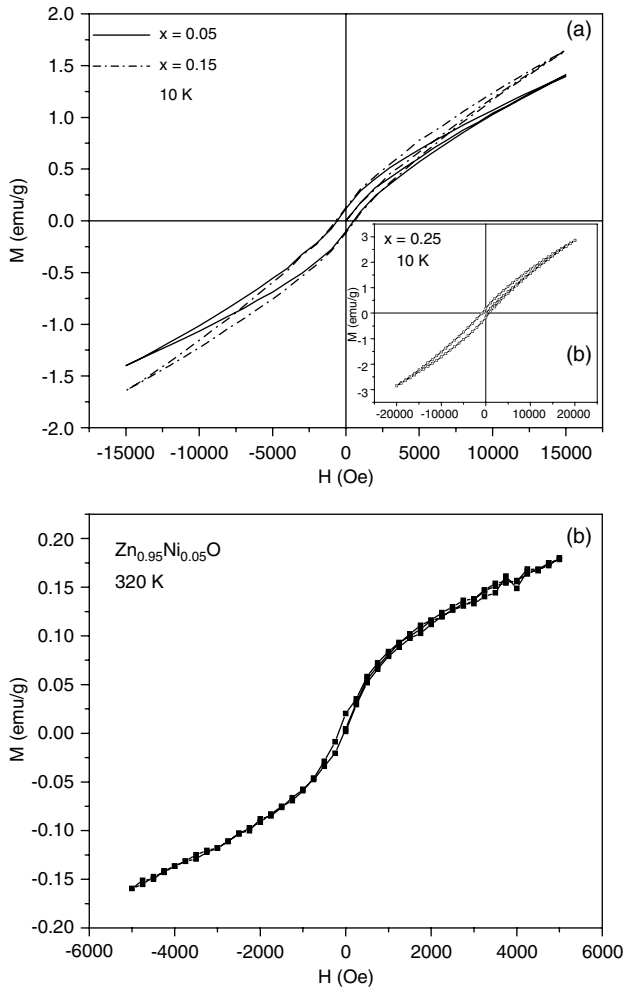

Figure 6. Field-dependent magnetization curves of $Zn_{1-x}Ni_xO$ compounds after calcination at 500 °C for 2 h for (a) $x = 0.05$, 0.15 and 0.25 (inset) at 10 K using SQUID and (b) $x = 0.05$ at 320 K using VSM.

direction so as to minimize the magneto-crystalline energy. However, polycrystalline samples contain particles in random orientation, and the net magnetic moment turns out to be very small or zero. Now, when a small magnetic field (say 500 Oe) is applied at a low temperature (10 K), the net magnetization gets essentially locked with particles having their easy axis around the applied field, aligning their moments along the field direction. As temperature increases, thermal energy becomes available to disturb the system, activating thereby the Zeeman interaction. Therefore, more moments begin to align with the external field direction in order to minimize the Zeeman energy term. Eventually, the net moment increases with temperature and passes through a maximum where all possible moments get aligned with the external field; the corresponding temperature is termed the blocking temperature (T_B). The magnetization versus temperature curve (figure 8) shows the blocking temperature (T_B) as 32 and 25 K for $x = 0.05$ and 0.15, respectively. Above T_B, thermal vibrations become strong enough to overcome the Zeeman interaction, and initiate randomization of the magnetic

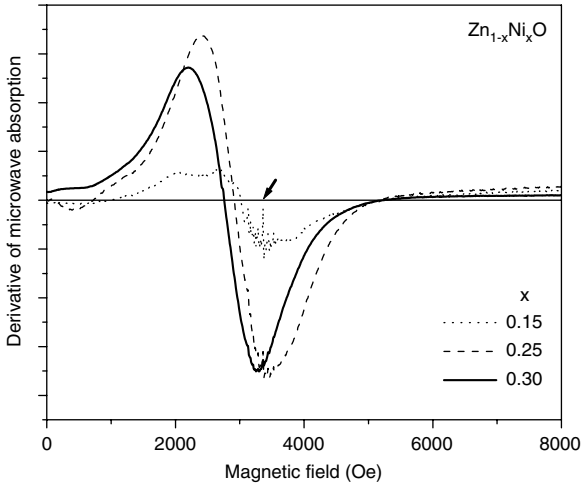

Figure 7. Room temperature ferromagnetic resonance (FMR) spectra of $Zn_{1-x}Ni_xO$ for $x = 0.15$, 0.25, and 0.30 at 9.451 GHz. The arrow indicates the resonance field for the free electron.

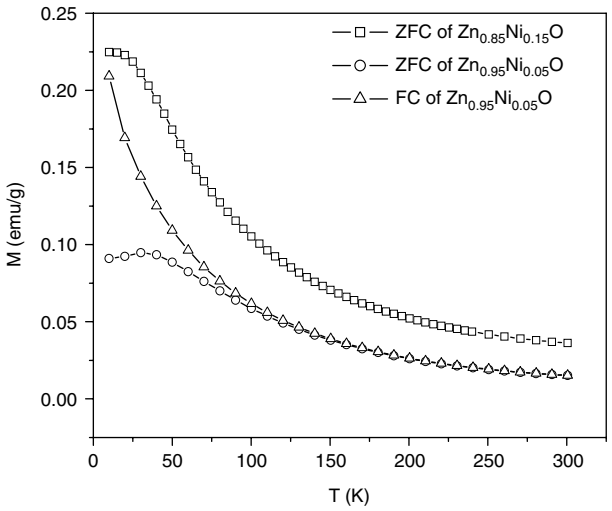

Figure 8. Temperature-dependent magnetization curves of $Zn_{1-x}Mn_xO$ compounds for $x = 0.05$ and 0.15 after calcination at 500 °C for 2 h under the zero field cooled (ZFC) condition recorded at 500 Oe. For the case of $x = 0.05$, the curve obtained under the FC condition is shown as well.

moments. This causes a continuous decrease in the magnetization value. Obviously, the nature of the M–T curve in $Zn_{1-x}Ni_xO$ confirms the presence of nanosized species. In the field cooled (FC) situation the external field is applied in both the cooling and heating processes. The net moment is measured during the heating cycle. In contrast to the ZFC case, the moments continue to progressively align themselves along the field direction during the cooling cycle. This leads to freezing of magnetic moments at low temperature. When heating is resumed and magnetization measurement performed with increase in temperature, the moment alignment tends to randomize and this reduces the net moment continuously (figure 8). Thus, M–T curves in ZFC and FC depict a deviation when samples contain nanosized magnetic particles

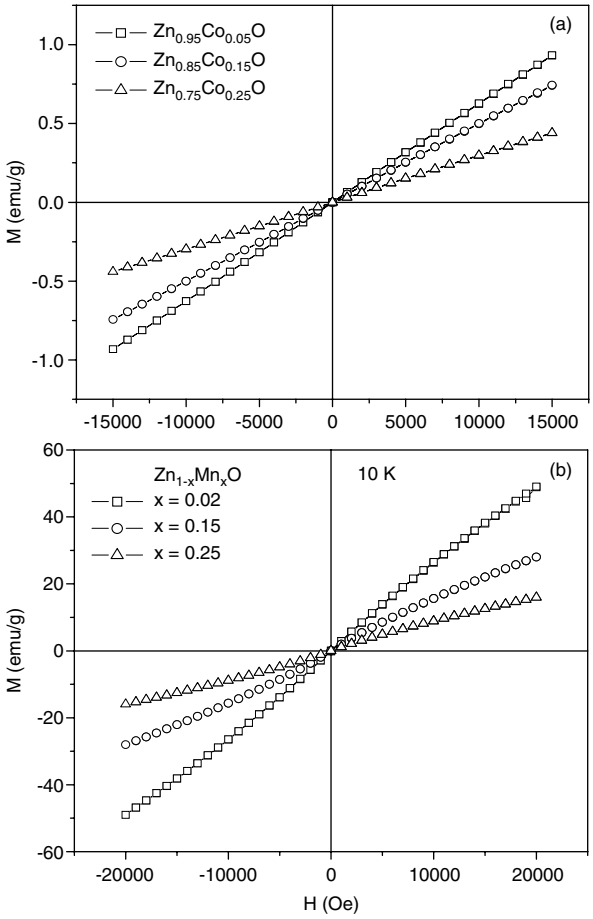

Figure 9. Field-dependent magnetization curves of (a) manganese and (b) cobalt containing ZnO of varying compositions at 10 K using SQUID.

of nickel containing ZnO; figure 8 clearly demonstrates this behaviour for $Zn_{1-x}Ni_xO$ system (notice the deviation occurring at 110 K for $x = 0.05$).

The magnetic behaviour of manganese and cobalt doped zinc oxide is very different. First, no hysteresis loops have been observed (figure 9). Second, the magnetization value decreases with increase in the Mn or Co content. Third, the M–T curves are identical under ZFC and FC conditions. Mn–Zn–O samples exhibit higher magnetization than cobalt containing ZnO; for example, for composition $x = 0.15$ the magnetization values at the field of 1.5 T are 20 and 6.65 emu g^{-1} at 10 K for $Zn_{1-x}Mn_xO$ and $Zn_{1-x}Co_xO$ system, respectively. Figure 10 shows inverse magnetic susceptibility curves as a function of temperature for $Zn_{1-x}Mn_xO$ system. The nature of the curve depicts ferrimagnetism (with Néel temperature $T_N = 4$ K) for $x = 0.02$, but antiferromagnetic characteristics for $x = 0.15$ and 0.25 with a Curie–Weiss temperature of -43 and -30 K, respectively, the corresponding transition temperature being 68 and 50 K, above which the behaviour is paramagnetic. These results are in variance with the recent observations in the $Zn_{1-x}Mn_xO$ ($x = 0.01$–0.05) compounds prepared by the solid state reaction method using high purity ZnO and MnO_2 powders [42, 43]. Accordingly, the magnetic behaviour is very sensitive to the preparation and annealing

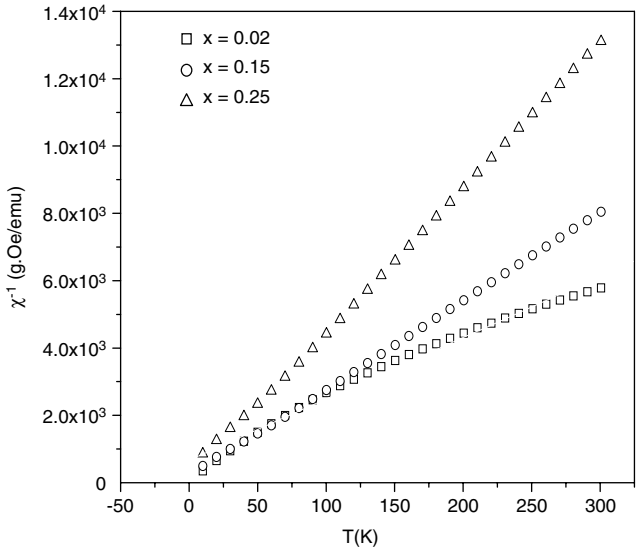

Figure 10. Inverse magnetic susceptibility versus temperature plot of $Zn_{1-x}Mn_xO$ compounds depicting ferrimagnetic nature with a Néel temperature of 4 K for $x = 0.02$ and antiferromagnetic characteristics with a Curie–Weiss temperature of -43 and -30 K for $x = 0.15$ and 0.25, respectively.

conditions; for example, while the samples sintered in air at 500 °C exhibit ferromagnetism at room temperature with a well defined hysteresis loop and considerable remanence and high coercivity, those sintered at 900 °C correspond to paramagnetic state. Further, the high temperature ferromagnetism is attributed to an oxygen vacancy stabilized metastable state phase of the form $Mn_{2-x}Zn_xO_{3-\delta}$, which transforms into a nonmagnetic Mn_3O_4 phase with oxygen uptake at ∼980 K, erroneously believed to be the Curie temperature. Obviously, the ferromagnetic phase essentially corresponds to a zinc doped Mn_2O_3 rather than the Mn doped ZnO. In contrast, a wurtzite hcp phase of Mn containing ZnO and a cubic $ZnMnO_3$ compound (when the Mn content is more than 10 at.%) are detected in the present work. That is perhaps the reason for not observing a ferromagnetic ordering of the above type in sol–gel processed $Zn_{1-x}Mn_xO$ powders.

The origin of ferromagnetism in DMSs is still a controversial subject. It is not yet clear whether the observed phenomenon is truly intrinsic or related to secondary phases such as magnetic clusters. Also, the magnetic properties observed so far are very sensitive to growth conditions and differ from sample to sample. Further, the first-principles pseudo-potential calculations and Monte Carlo simulations have shown that the hydrogen present in Zn–Co–O can (i) produce stable cobalt dimmers on nearest-neighbour zinc sites, (ii) bind the comprising species strongly, and (iii) directly mediate a strong spin–spin interaction leading to high temperature ferromagnetism [11, 44]. Needless to say, a significant amount of unintended hydrogen impurity is always present interstitially in ZnO or Zn–Co–O [44]. The various models proposed to explain the origin of ferromagnetism in DMSs include direct exchange interaction (i.e., coupling of spins of localized electrons), super-exchange interaction mediated by intermediate anions, carrier-mediated exchange of localized magnetic moments (RKKY, Zener carrier-mediated, and Zener double-exchange interactions) and strong interaction of bound magnetic polarons [5, 45, 46]. Venkatesan *et al* [45] have proposed a spin-split donor impurity-band model for ferromagnetism in high-k dielectric oxides doped with a few per cent

of transition metal ions. Accordingly, high Curie temperatures result whenever unoccupied 3d states of magnetic species overlap the spin-split band of the donor impurity. For cobalt, the $3d^{\downarrow}$ states lie high in the 2p (O)–4s (Zn) gap and overlap with the impurity band which itself is spin-split (the Fermi level being within the band). This results in a strong exchange interaction and a net magnetic moment. The likely donor impurities in ZnO thin films are oxygen vacancies and the localized electrons in the impurity band bring about ferromagnetic coupling when the localization length is at least γa_0 ($\gamma = km_e/m^*$), where a_0 is the Bohr radius, k is the high frequency dielectric constant, m_e is the electron mass and m^* is the electron effective mass; the value of γ is 14 for ZnO. In recent studies [46, 47], pellets of composition x mol% MnO_2–$(1 - x)$ mol% ZnO ($x = 2$, 10) after annealing at 500 °C are found to exhibit room temperature ferromagnetism. The origin is, however, explained on the basis of a new approach involving diffusion of Zn^{2+} ions into nanosize MnO_2 grains (rather than manganese in ZnO), the emergence of Mn^{3+} ions due to partial reduction of Mn^{4+} ions, and a double-exchange mechanism as reported in other systems having coexistence of Mn^{3+} and Mn^{4+} ions and displaying ferromagnetic ordering with high Curie temperatures [48]. Obviously, elucidation of the mechanism responsible for ferromagnetism in DMSs is still an open issue and requires further work. Our experiments are also underway to determine the conditions leading to ferromagnetic ordering in ZnO based DMSs; these will be reported in due course together with possible mechanism(s).

4. Conclusions

Transition metal containing nanocrystalline ZnO powders synthesized by the sol–gel process correspond to a wurtzite hcp structure similar to that of pure ZnO ($a = 3.248$ Å, $c = 5.203$ Å), but with the lattice parameters varying slightly with type and extent of doping. The phases that appear beyond the dissolution limit (being 10 at.% for Ni and Co, 10–15 at.% for Mn) are NiO (hexagonal, $a = 2.954$ Å, $c = 7.236$ Å), $ZnCo_2O_4$ (cubic, $a = 8.095$ Å) and $ZnMnO_3$ (cubic, $a = 8.25$ Å). While the gel displays filter paper like fibrous network morphology, the oxalate contains needles having either the disposition of nanoparticles along their lengths or sharp boundaries. $Zn_{1-x}Ni_xO$ exhibits ferromagnetism at room temperature as indicated by the hysteresis loops and gradual shift in the ESR spectra towards lower resonance field (H_r) with increase in nickel content (x) (a typical g-factor value being 2.317 for x equal to 0.25). However, the magnetic characteristics of manganese and cobalt containing ZnO show a decrease of magnetization with rise of doping level and no hysteresis loops. $Zn_{1-x}Mn_xO$ compounds reveal ferrimagnetism for $x = 0.02$ (Néel temperature $T_N \sim 4$ K), but antiferromagnetism for $x = 0.15$ and 0.25 with a Curie–Weiss temperature of -43 and -30 K, respectively. Magnetization versus temperature curves under zero field cooled and field cooled conditions deviate in the $Zn_{1-x}Ni_xO$ system (the blocking temperature T_B being 32 K for $x = 0.05$), but they remain identical in the case of manganese and cobalt containing ZnO.

References

[1] Gregg J F, Petej I, Jouguelet E and Dennis C 2002 *J. Phys. D: Appl. Phys.* **35** R121–55
[2] Sarma S D, Fabin J, Hu X and Žutić I 2000 *IEEE Trans. Magn.* **36** 2821–6
[3] Dietl T, Ohno H, Matsukura F, Cibert J and Ferrand D 2000 *Science* **287** 1019
[4] Dietl T 2002 *Semicond. Sci. Technol.* **17** 377–92
[5] Janisch R, Gopal P and Spaldin N A 2005 *J. Phys.: Condens. Matter* **17** R657–89
[6] Furdyna J K 1998 *J. Appl. Phys.* **64** R29
[7] Fukumura T, Toyosaki H and Yamada Y 2005 *Semicond. Sci. Technol.* **20** S103–11

[8] Pearton S J, Norton D P, Ip K, Heo Y W and Steiner T 2005 *Prog. Mater. Sci.* **50** 293–340
[9] Pearton S J, Heo W H, Ivill M, Norton D P and Steiner T 2004 *Semicond. Sci. Technol.* **19** R59–74
[10] Fukumura T, Yamada Y, Toyosaki H, Hasegawa T, Koinuma H and Kawasaki M 2004 *Appl. Surf. Sci.* **223** 62–7
[11] Sato K and Katayama-Yosida H 2001 *Japan. J. Appl. Phys.* **40** L651–3
[12] Ohno H, Shen A, Matsukura F, Oiwa A, Endo A, Katsumoto S and Iye Y 1996 *Appl. Phys. Lett.* **69** 363–5
[13] Pearton S J, Abernathy C R, Overberg M E, Thaler G T, Norton D P, Theodoropoulou N, Hebard A F, Park Y D, Ren F, Kim J and Boatner L A 2003 *J. Appl. Phys.* **93** 1
[14] Sarma S D, Hwang E H and Kaminski A 2003 *Phys. Rev.* B **67** 155201–16
[15] Sharma P, Gupta A, Rao K V, Owens F J, Sharma R, Ahuja R, Guillen J M O, Johansson B and Gehring G A 2003 *Nat. Mater.* **2** 673–7
[16] Sharma P, Gupta A, Owens F J, Inoue A and Rao K V 2004 *J. Magn. Magn. Mater.* **282** 115–21
[17] Heo Y W, Ivill M P, Ip K, Norton D P and Pearton S J 2003 *Appl. Phys. Lett.* **84** 2292–4
[18] Fukumura T, Jin Z, Kawasaki M, Shono T, Hasegawa T, Koshihara S and Koinuma H 2001 *Appl. Phys. Lett.* **78** 958–60
[19] Jung S W, An S-J, Yi G-C, Jung C U, Lee S-I and Cho S 2002 *Appl. Phys. Lett.* **80** 4561–3
[20] Yoon S W, Cho S-B, We S C, Yoon S, Suh B J, Song H K and Shin Y J 2003 *J. Appl. Phys.* **93** 7879–81
[21] Kim J H, Choo W K, Kim H, Kim D and Ihm Y E 2003 *J. Korean Phys. Soc.* **42** S258–62
[22] Kim S S, Moon J H, Lee B-T, Song O S and Je J H 2004 *J. Appl. Phys.* **95** 454–9
[23] Ando K, Saito H, Jin Z, Fukumura T, Kawasaki M, Matsumoto Y and Koinuma H 2001 *Appl. Phys. Lett.* **78** 2700–2
[24] Jin Z, Fukumura T, Kawasaki M, Ando K, Saito H, Sekiguchi T, Yoo Y Z, Murakami M, Matsumoto Y, Hasegawa T and Koinuma H 2001 *Appl. Phys. Lett.* **78** 3824–6
[25] Norton D P, Pearton S J, Hebard A F, Theodoropoulou N, Boatner L A and Wilson R G 2003 *Appl. Phys. Lett.* **82** 239–41
[26] Radovanovic P V and Gamelin D R 2003 *Phys. Rev. Lett.* **91** 157202–4
[27] Radovanovic P V, Norberg N S, McNally K E and Gamelin D R 2002 *J. Am. Chem. Soc.* **124** 15192–3
[28] Norberg N S, Kittilstved K R, Amonette J E, Kukkadapu R K, Schwartz D A and Gamelin D R 2004 *J. Am. Chem. Soc.* **126** 9387–98
[29] Kittilstved K R and Gamelin D R 2005 *J. Am. Chem. Soc.* **127** 5292–3
[30] Lee H-J, Jeong S-Y, Cho C R and Park C H 2002 *Appl. Phys. Lett.* **81** 4020–2
[31] Cong C J, Liao L, Li J C, Fan L X and Zhang K L 2005 *Nanotechnology* **16** 981–4
[32] Pillai S C, Kelly J M, McCormack D E, O'Brien P and Ramesh R 2003 *J. Mater. Chem.* **13** 2586–90
[33] Pillai S C, Kelly J M, McCormack D E and Ramesh R 2004 *J. Mater. Chem.* **14** 1572–8
[34] Shen R J, Jia D Z, Qiao Y M and Wang J Y 2001 *J. Inorg. Mater.* **16** 625
[35] Guo L, Ji Y, Xu H, Wu Z and Simon P 2003 *J. Mater. Chem.* **13** 754
[36] Brinker C J and Sherer G W 1990 *Sol–Gel Science: the Physics and Chemistry of Sol–Gel Processing* (San Diego, CA: Academic) p 908
[37] Galasso F S (ed) 1970 *Structure and Properties of Inorganic Solids* vol 7 (Oxford: Pergamon) p 122
[38] Shannon R D 1976 *Acta Crystallogr.* A **32** 751–67
[39] Ueda K, Tabata H and Kawai T 2001 *Appl. Phys. Lett.* **79** 988–90
[40] Yang L W, Wu X L, Huang G S, Qiu T and Yang Y M 2005 *J. Appl. Phys.* **97** 014308
[41] Mofor A C, El-Shaer A, Bakin A, Waag A, Ahlers H, Siegner U, Sievers S, Albrecht M, Schoch W, Izyumskaya N, Avrutin V, Sorokin S, Ivanov S and Stoimenos J 2005 *Appl. Phys. Lett.* **87** 062501–3
[42] Zhang J, Skomski R and Sellmyer D J 2005 *J. Appl. Phys.* **97** 10D303
[43] Kundaliya D, Ogale S, Lofland S, Dhar S, Metting C, Shinde S, Ma Z, Varughese B, Ramanujachary K, Salamanca-Riba L and Venkatesan T 2004 *Nat. Mater.* **3** 709–14
[44] Park C H and Chadi D J 2005 *Phys. Rev. Lett.* **94** 127204
[45] Venkatesan M, Fitzgerald C B, Lunney J G and Coey J M D 2005 *Phys. Rev. Lett.* **93** 177206
[46] García M A *et al* 2005 *Phys. Rev. Lett.* **94** 217206
[47] Costa-Kramer J L *et al* 2005 *Nanotechnology* **16** 214–8
[48] Salamon M B and Jaime M 2001 *Rev. Mod. Phys.* **73** 583–628